ACS APPLIED MATERIALS & INTERFACES

RESEARCH ARTICLE

www.acsami.org

New Generation Photocatalysts: How Tungsten Influences the Nanostructure and Photocatalytic Activity of TiO_2 in the UV and Visible Regions

Václav Štengl,* Jana Velická, Monika Maříková, and Tomáš Matys Grygar

Department of Solid State Chemistry, Institute of Inorganic Chemistry AS CR v.v.i., 250 68 Řež, Czech Republic

Supporting Information

ABSTRACT: Tungsten-doped anatase was prepared by a thermal hydrolysis of aqueous solutions of peroxo complexes of titanium and tungsten. The synthesized samples included X-ray diffraction, high-resolution transmission electron microscopy, selected area electron diffraction, Raman spectroscopy, specific surface area, and porosity determination. W doping resulted in a decrease of the unit-cell volume of anatase at lower W contents and an increase at higher W contents. The position of the most intense Raman band of the E_g mode (near 147 cm^{-1}) also has a local minimum at medium-doped titania (1.1−3.6% W in titania). W doping increases the temperature of anatase-to-rutile transformation by about 100 °C compared with nondoped anatase. The photocatalytic activity of doped titania samples was determined by decomposition of Orange II dye during irradiation at 365 and 400 nm. Specimens with moderate W doping (1.0−3.3% W) perform best: they enhance the corresponding reaction rates 10 times at 365 nm and 5 times at 400 nm, respectively, compared with pure titania obtained under the same set of synthesis conditions.

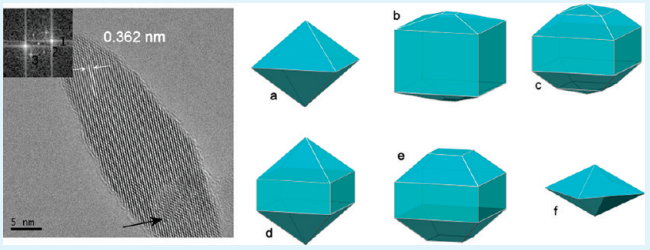

KEYWORDS: titania, peroxo complexes, tungstate, thermal hydrolysis, photocatalysis

1. INTRODUCTION

Titanium dioxide is currently the most important, most widespread, and most investigated photocatalyst because of its optical and electronic properties, chemical stability, nontoxicity, and potential application in the decomposition of many organic pollutants present in liquid or gaseous phases. Its massive expansion in applications is obstructed primarily by its high cost and its activity limited to the UV region, which allows it to utilize only about 3% of the solar radiation. The cost of only part of the commercially available photocatalysts based on TiO_2 is relatively high, 99 €/100 g (P25).

Published procedures for the preparation of TiO_2 for the UV and visible regions of light are often titanium organometallic compounds used as a feedstock, such as, for example, titanium(IV) isopropoxide $Ti[OCH(CH_3)_2]_4$ or titanium(IV) butoxide $Ti[O(CH_2)_3CH_3]_4$. Another frequently used starting compound is $TiCl_4$, the high reactivity and exothermal reaction with water and acids of which make its handling difficult.

The precursors of WO_3-doped TiO_2 nanocrystallites were formulated by a sol−precipitation method and calcined at temperatures ranging from 400 to 900 °C for 2 h in air.[1] Nanocrystalline W-doped titanium dioxide powders were prepared by a sol−gel method based on hydrolysis of $TiCl_4$ in aqueous solution. W doping was added to extend the light absorption of the resulting TiO_2-based photocatalysts toward the visible light range.[2] Sol−gel-prepared W^{VI}-doped TiO_2 powders prepared from titanium(IV) isopropoxide and ammonium tungstate $[(NH_4)_{10}W_{12}O_{41}\cdot 7H_2O]$ were evaluated as photocatalysts for crystal violet bleaching under UV irradiation in the presence of O.[3] W-modified titanium dioxide catalysts prepared by sol−gel methods and obtained commercially were compared for their photocatalytic activity using mechanistic probes designed to examine chemical pathways of oxidation.[4]

Tungstated titania catalysts were also prepared by wet impregnation of hydrous titanium oxide. With increasing W loading, the surface area increases and TiO_2 particle sizes and pore diameters decrease. When the W loading exceeds 20 wt % WO_3 and the calcination temperature exceeds 650 °C, WO_3 is formed.[5] TiO_2−WO_3 photocatalysts were prepared in a vacuum evaporator by impregnation of TiO_2 with WO_2 dissolved in a solution of H_2O_2 (30%) and followed by calcination at 400 and 600 °C.[6] Catalysts based on titania mixed with tungstophosphoric acid $H_3PW_{12}O_{40}$, in various proportions (1, 15, 25, and 50 wt %) were obtained by the sol−gel method.[7] TiO_2 thin films were prepared using the dip-coating method with a polymeric sol including additives, such as Al, W, and Al + W, to examine two major properties: photocatalysis and hydrophilicity. W-doped films exhibited the best photocatalytic efficiency, while aluminum-doped films were poorer than undoped samples.[8] A WO_3-doped TiO_2 nanotube thin film was fabricated by anodizing the TiO_2 nanotube film in an NH_4F electrolyte containing WO_4 ions.[9]

Acidification of an isopropyl alcohol solution containing mixtures of $[Ti(OPr)_4]$- and $[W(OEt)_5]$-produced solutions from

Received: July 4, 2011
Accepted: September 26, 2011
Published: September 26, 2011

Table 1. Characteristics of Prepared Titania Samples Doped by Variable Amounts of Tungsten

sample	$NaWO_4 \cdot 2H_2O$ [g]	W [%]	W/Ti molar ratio	crystallite size [nm]	BET [$m^2\ g^{-1}$]	total pore volume [$cm^3\ g^{-1}$]	micropore surface area [$m^2\ g^{-1}$]	micropore volume [$cm^3\ g^{-1}$]	cell param a [Å]	cell param c [Å]
TiW000				26.0	145.0	0.6963	3.810	0.00099	3.796	9.511
TiW005	0.050	0.53	0.0023	23.2	181.9	0.551	0.718	0	3.794	9.512
TiW010	0.100	1.02	0.0045	22.7	100.6	0.337	5.880	0.00214	3.793	9.512
TiW015	0.150	1.87	0.0084	35.9	118.9	0.281	5.695	0.00185	3.793	9.512
TiW017	0.175	1.13	0.0050	14.9	125.3	0.298	0	0	3.791	9.503
TiW020	0.200	2.09	0.0093	39.6	93.4	0.604	0	0	3.793	9.513
TiW022	0.225	1.87	0.0083	20.8	161.2	0.694	0	0	3.792	9.507
TiW025	0.250	2.54	0.0162	13.4	128.2	0.252	0	0	3.794	9.500
TiW030	0.300	3.37	0.0148	34.6	151.7	0.874	0	0	3.793	9.510
TiW050	0.500	3.17	0.0143	18.1	119.2	0.282	0	0	3.793	9.505
TiW100	1.000	6.45	0.0305	25.1	104.2	0.352	0	0	3.794	9.502
TiW125	1.125	9.41	0.0464	15.5	212.0	0.389	0	0	3.797	9.495
TiW150	1.500	10.79	0.0543	13.6	241.3	0.405	0	0	3.798	9.493
TiW175	1.175	12.68	0.0656	13.3	193.3	0.345	0	0	3.800	9.493
TiW200	2.000	16.94	0.0937	17.4	116.7	0.251	0	0	3.802	9.481

which various TiO_2, WO_3, and TiO_2/WO_3 thin films could be obtained by dip coating and annealing.[10] Mesoporous W^{VI}-doped TiO_2 thin-film photocatalysts were prepared via electrospinning and sol−gel chemistry, employing a triblock copolymer as a structure-directing agent. The photocatalytic activity of the films was investigated by employing methylene blue and 3 wt % as the most suitable content of W^{VI} in TiO_2.[11] Monolayer coverage of highly acidic semiconductors, such as MoO_3 and WO_3 on the surface of TiO_2 nanoparticles (Degussa P25), would improve greatly the stability of colloidal suspensions in an aqueous solution, and the photocatalytic activity of these WO_3/TiO_2 films is 2.8−3 times that of a pure TiO_2 film in decomposing gas-phase 2-propanol, while the MoO_3/TiO_2 film is less effective.[12]

The aim of this paper is to study the influence of the incorporation of W into monodisperse anatase by using a synthesis route much simpler than previous ones. A total of 11 samples labeled TiW005−TiW100 were prepared using "one-pot" thermal hydrolysis of aqueous titanium and tungsten peroxo complexes based on our original procedure.[13] The photocatalytic activity of the as-prepared doped titania was assessed by the photocatalytic decomposition of Orange II dye in an aqueous slurry under irradiation at wavelengths of 365 and 400 nm.

According to the degradation pathway proposed in ref 14, the main byproducts formed by the ozonation of azo dye are organic acids, aldehydes, and ketones, with the final product being carbon dioxide. Demirev and Nenov[15] suggested that the eventual degradation products of azo dye in the ozonation system would be acetic, formic, and oxalic acids. The reaction pathway for the visible-light-driven photocatalytic degradation of Orange II dye in aqueous TiO_2 suspensions is shown schematically in 16. Its degradation is very easily monitored by an experimental apparatus (see the Experimental Section), and hence it is a very simple surrogate for organic pollutants, of which degradation is one of the main strategic goals of titania research.

2. EXPERIMENTAL SECTION

2.1. Synthesis of W-Doped Titania. All chemicals used—titanium oxosulfate ($TiOSO_4$), sodium tungstate dihydrate ($Na_2WO_4 \cdot 2H_2O$), ammonium hydroxide (NH_4OH), and hydrogen peroxide (H_2O_2)—were of analytical grade and were supplied by Sigma-Aldrich Company Ltd., Gillingham, Dorset, U.K.

In a typical experiment, 100 mL of a 1.2 M solution of titanium oxosulfate was diluted with distilled water to a volume of 2 L and hydrolyzed by the slow addition of an ammonium hydroxide solution (10%) under constant stirring at a temperature of 0 °C in an ice bath until the reaction mixture reached pH 8.0. The obtained white precipitate was separated by filtration and washed with distilled water until it was free of sulfate ions (confirmed by a $BaCl_2$ test). The obtained wet precipitate was mixed with 100 mL of a 30% hydrogen peroxide solution, which produced a homogeneous yellow gelatinous mass. That mass was subsequently mixed with a defined amount of sodium tungstate dihydrate ($Na_2WO_4 \cdot 2H_2O$) dissolved in 10 mL of H_2O_2 (see Table 1 for the stoichiometry) and refluxed in a round-bottomed flask in a heating mantle. During heating, a yellowish white precipitate was formed. Refluxing continued until the precipitate changed its color to white (at low W content) or yellowish (at high W content), i.e., for ∼36 h. The obtained doped titania was air-dried at 105 °C.

2.2. Characterization Methods. Diffraction patterns were collected with a PANalytical ẊPert PRO diffractometer equipped with a conventional X-ray tube (Cu Kα radiation, 40 kV, 30 mA) and a PIXcel linear position-sensitive detector with an antiscatter shield. A programmable divergence slit set to a fixed value of 0.5°, Soller slits of 0.02 rad, and a mask of 15 mm were used in the primary beam. A programmable antiscatter slit set to a fixed value of 0.5°, a Soller slit of 0.02 rad, and a Ni β filter were used in the diffracted beam. The phase identification was performed with the DiffracPlus Eva software package (Bruker AXS GmbH, Karlsruhe, Germany) using the JCPDS PDF-2 database.[17] For the quantitative phase analysis, *DiffracPlus Topas*, version 4.1 (Bruker AXS, Göttingen, Germany), was used with structural models taken on the ICSD database.[18] The latter program employs a Rietveld refinement procedure that allows estimation of the weight fractions of the crystalline phases and their lattice sizes and mean coherence lengths. The sample TiW200 was studied by in situ high-temperature X-ray diffraction (XRD) in air with a PANalytical X'PertPRO diffractometer using Co K radiation (40 kV, 30 mA) and a X'Celerator multichannel detector with an antiscatter shield, equipped with a high-temperature chamber (HTK 16; Anton Paar GmbH, Graz, Austria). The measurements were started at room temperature and completed at 1200 °C.

Transmission electron microscopy (TEM and HRTEM) micrographs were obtained using a JEOL JEM 3010 microscope operated at

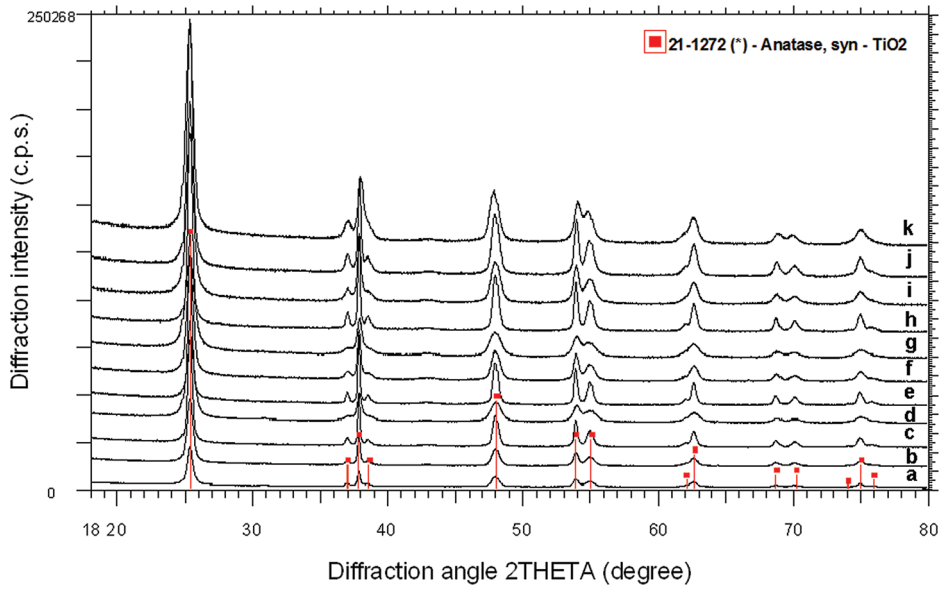

Figure 1. PXRD patterns of W-doped titania: (a) TiW005, (b) TiW010, (c) TiW015, (d) TiW017, (e) TiW020, (f) TiW022, (g) TiW025, (h) TiW030, (i) TiW050, (j) TiW100, and (k) TiW200.

300 kV (LaB_6 cathode). A copper grid coated with a holey carbon support film was used to prepare samples for TEM observation. The powdered sample was dispersed in ethanol and the suspension treated in an ultrasonic bath for 10 min.

The specific surface areas of samples were determined from nitrogen adsorption−desorption isotherms at liquid-nitrogen temperature using a Coulter SA3100 instrument with 15 min of outgas at 150 °C. The Brunauer−Emmett−Teller (BET) method was used for surface area calculation,[19] and the pore-size distribution (pore diameter, pore volume, and micropore surface area of the samples) was determined by the Barrett−Joyner−Halenda (BJH) method.[20]

Diffuse-reflectance UV/vis spectra for evaluation of the photophysical properties were recorded in the diffuse-reflectance mode and transformed to absorption spectra through the Kubelka−Munk function.[21] A Perkin-Elmer Lambda 35 spectrometer equipped with a Labsphere RSAPE- 20 integration sphere with $BaSO_4$ as a standard was used.

Raman spectra were obtained with a DXR Raman microscope (Thermo Fisher Scientific,Waltham, MA). A 532 nm laser was used at a power of 3 mW. Powdered samples were scanned at 15-point mapping mode under a 10× objective with an automated autofocus at each point to get 15 random measurements.

Element analysis was performed by an energy-dispersive X-ray fluorescence spectrometer (MiniPal 4.0; PANalytical, Eindhoven, The Netherlands) with a Rh lamp and a Peltier-cooled Si PIN detector. Powdered samples were poured into plastic cells with Mylar foil bottoms with diameter 25 mm. Analysis was performed by "standardless" measurements and a calculation procedure based on the first principles of X-ray fluorescence.

The photocatalytic activity was assessed from the kinetics of the photocatalytic degradation of Orange II dye (sodium salt 4-[(2-hydroxy-1-naphtenyl)azo]benzenesulfonic acid) in aqueous slurries. In contrast to methylene blue, the azo dyes (Orange II, Methyl Red, Congo Red, etc.) are not absorbed on titania surfaces and, hence, their photodecomposition is evaluated simply from the concentration of the remaining dissolved dye. For the azo dye degradation, the complete mass balance in nitrogen indicated that the central −N═N− azo group is converted into N_2, which is ideal for the elimination of nitrogen-containing pollutants not only for environmental photocatalysis but also for any physicochemical method.[22] Direct photolysis by UV light or solar radiation cannot mineralize Orange II.[23] The kinetics of photocatalytic degradation of an aqueous Orange II dye solution was measured by using a self-constructed photoreactor.[24] It consists of a stainless steel cover and a quartz tube with a Narva fluorescent lamp having a power of 13 W and a light intensity of ∼3.5 mW cm^{-2}. Black-light (365 nm) for UV and warm white lamps (on 400 nm) for visible-light irradiation were used. A total of 1 L of a 0.5 mM Orange II dye solution was circulated by means of a membrane pump through a flow-through measuring cell. The concentration of Orange II dye was determined by measuring the absorbance at 480 nm with a ColorQuestXE visible-light spectrophotometer. The 0.5 g of a titania sample was sonicated for 10 min with an ultrasonic bath (300 W and 35 kHz) before the kinetic tests. The pH of the resulting suspension was taken as the initial value for neutral conditions and kept at a value of 7.0 in the experiment.

3. RESULTS AND DISCUSSION

3.1. Structural Changes by W Doping. The PXRD patterns of the W-doped titania samples are shown in Figure 1. Only the diffraction lines of anatase (ICDD PDF 21-1272) can be seen. Table 1 shows the crystallite size and cell parameters *a* and *c* of the anatase calculated by Rietveld refinement; the former dependence is also depicted in Figure 2.

The high-temperature XRD diffractogram of sample TiW200 is depicted in Figure S1 in the Supporting Information. The measurement started at room temperature and was completed at 1200 °C with 100° steps at temperatures of 25−550 °C and 25 °C steps at 550−1200 °C. Anatase (ICDD PDF 21-1272) and rutile (ICDD PDF 21-1276) were observed during heating. No diffraction lines of W compounds or other phases were observed at temperatures of up to 825 °C (except for platinum sample holder diffraction lines), which means that W is either noncrystalline (amorphous) or incorporated into the anatase structure.

Temperatures above 800 °C lead to the formation of crystalline WO_3 (ICDD PDF 89-1287), and from 975 °C, it is incorporated into the rutile structure, as already described.[25] The anatase-to-rutile phase transformation begins at a higher temperature than nondoped anatase; it starts at 900 °C and

continues up to 1125 °C (see Figure S2a in the Supporting Information), which is about 125 °C higher than that of pure anatase[26] and 100 °C higher than that of Mo-doped titania.[27]

As previously noted, the thermodynamic stability of titania polymorphs depends on the crystallite size.[28] The temperature of the transition between the two phases is also the temperature at which a critical crystallite size is achieved. The dependence of the crystallite size on the temperature (see Figure S2b in the Supporting Information) shows that the phase transition of anatase begins at the threshold crystallite size of about 50 nm. Compared with the results,[29] the temperature shift by ∼100 °C for the phase transition of anatase to rutile is associated with a faster growth of the anatase crystallite size.

The unit-cell sizes of the sample TiW200 prepared by in situ heating experiments increase almost linearly, which reflects thermal expansion of the structures (see Figure S2c,d in the Supporting Information). An exception is the unit-cell parameter *a* of anatase, which decreases slightly with an increase in the temperature up to 400 °C. This reduction is probably caused by the evolution of physically and chemically bounded water.

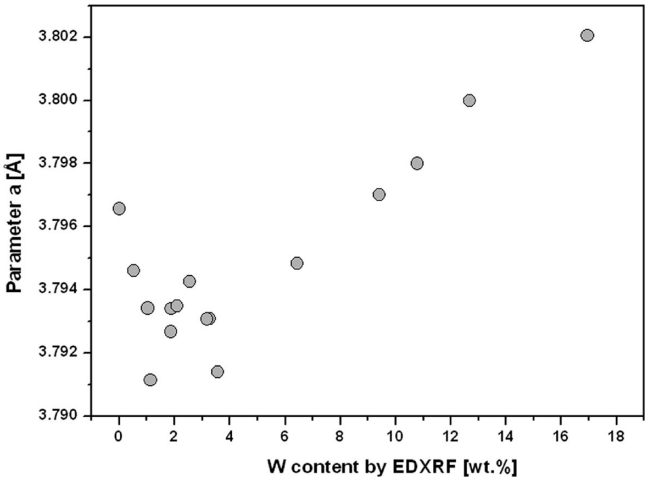

Figure 2. Dependence of the lattice parameter *a* on the W content.

At temperatures above 800 °C, the cell parameter *a* of anatase decreases, which is caused by the release of W from the anatase structure and the subsequent anatase-to-rutile transformation.

Raman spectroscopy confirmed that the prepared W-doped titania is pure anatase. The position of the most intensive Raman band, the E_g transition close to 147 cm^{-1}, changes with W doping in a nonmonotonous way (see Figure 3), just as do the unit-cell volume V_{cell} and the lattice parameter *a* obtained by XRD (Figure 2). The unit-cell parameters and Raman band shifts, hence, clearly show two different ways of introducing W into the anatase crystal: at low W concentrations, *a*, V_{cell}, and the main Raman band position decrease because all of these parameters reach corresponding local minima at ∼2% W rather than at larger W contents when these parameters grow.

The ionic radius of W^{6+} is 0.060 nm,[29] and that of Ti^{4+} is 0.0605 nm.[30] Because of such a close similarity, W can easily be introduced into the TiO_2 lattice, but, on the other hand, the observed changes of the anatase unit-cell size due to that substitution are quite surprising. In fact, all specimens expand the lattice size with respect to pure anatase with *a* = 3.782 Å and *c* = 9.502 Å,[31] which is caused by two different effects: First, a structural nonstoichiometry, expanding the lattice by about 0.3%, because anatase was prepared by a soft synthesis, usually producing a certain portion of OH^- groups compensated for by cation vacancies (instead of regular O^{2-} and a fully occupied cationic lattice); this fact is indirectly proven by the anatase lattice cell shrinking observed during high-temperature XRD measurements. The second is a minor specific effect of W doping existing as shown by trends in Figure 2. The second effect might seem less relevant and close to the reliability limits of the analytical techniques; however, the Raman band position (Figure 3) changes in

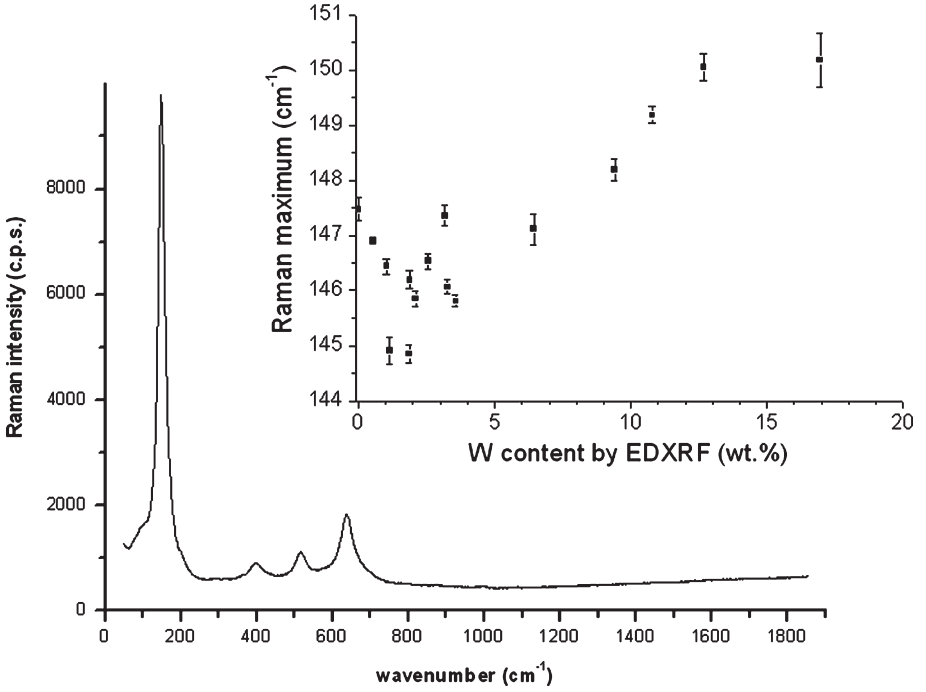

Figure 3. Raman spectrum of sample TiW025. Inset: dependence of the position of the maximum of the main E_g band on the W content in titania.

a manner very similar to that of the *a* lattice parameter (Figure 2). Actually, the agreement of the results of these two fundamentally different methods (XRD and Raman) confirms that W doping causes some structural differences and that there are some fundamental differences between lower and higher W-doped titania specimens.

Recently, we reported on a nonmonotonous change of the lattice parameters in Mo-doped titania,[27] which has also been accompanied by a dependence of the Mo valence on the Mo percentage. In the Mo case, Mo^{V} increased with growing Mo doping at low Mo contents, and then only Mo^{VI} was introduced. In W-doped titania, the W valence does not appear to be variable because none of the W-doped titania specimens has a bluish hue, which could have been attributed to W^{V}. On the other hand, the nonmonotonous dependence of the structural features of W-doped anatase could be assigned to microstructural changes of the anatase lattice by the insertion of W ions, which Kamisaka et al. have discussed recently.[31] Their density functional theory calculations show that certain structural motifs of W^{6+} and/or W^{6+} and O vacancies cause a variable anisotropic distortion of the anatase lattice on the order of about 0.1% of the cell size. This extent is comparable to the W-content specific defect, which we observed in the W-doped titania (Figure 2).

Figure S3 in the Supporting Information shows the IR spectrum of the W-doped titania prepared by thermal hydrolysis of titania peroxo complexes. The broad absorption peaks about 3400 cm^{-1} and the band at 1631 cm^{-1} correspond to the surface-absorbed water and the hydroxyl groups.[32] Both observed peaks are recognized as an important factor affecting the photocatalytic activity.[33] The small peak at ~1380 cm^{-1} can be assigned to surface carbonates formed by the adsorption of atmospheric CO_2.[34] Low-frequency bands in the range <500 cm^{-1} correspond to the Ti−O−Ti vibration of the network.[35] A small amount of sulfate ions adsorbed on the surface can be inferred from a band around ~1115 cm^{-1} (sulfates[36]).

3.2. Surface Areas, Porosity, and Microstructure. The specific surface area of the as-prepared samples, calculated by the multipoint BET method, total pore volume, micropore surface area, and micropore volume are listed in Table 1. The BJH pore-size distribution plot and nitrogen adsorption−desorption isotherms (inset) of as-prepared samples are shown in Figure S4 in the Supporting Information. According to the IUPAC notation,[37] microporous materials have pore diameters of >2 nm and macroporous materials of >50 nm; the mesoporous category thus lies in the middle. The mean pore size of the W-doped titania is in the range of 10−20 nm with a relatively narrow size distribution. All samples have a type IV isotherm, characteristic of mesoporous material with type H2 hysteresis of large-pore mesoporous materials; they can be ascribed to capillary condensation in the mesopores. The high steepness of the hysteresis indicates a high order of mesoporosity. All samples are characteristic of type A hysteresis loop according to the de Boer classification.[38] This hysteresis type is connected with pores in the form of capillary tubes open at both ends, wide ink-bottle pores, and wedge-shaped capillaries. The samples TiW05, TiW010, and TiW015 also have microporous texture and micropore surface areas of 0.718, 5.880, and 5.695 $m^2\ g^{-1}$. The presence of micropores in these samples is likely to have a negative effect on the photocatalytic activity.

The selected area electron diffraction (SAED) patterns analyzed by the *Process Diffraction* program produced a structure of all samples, which is anatase (ICDD PDF 21-1272). The aspect

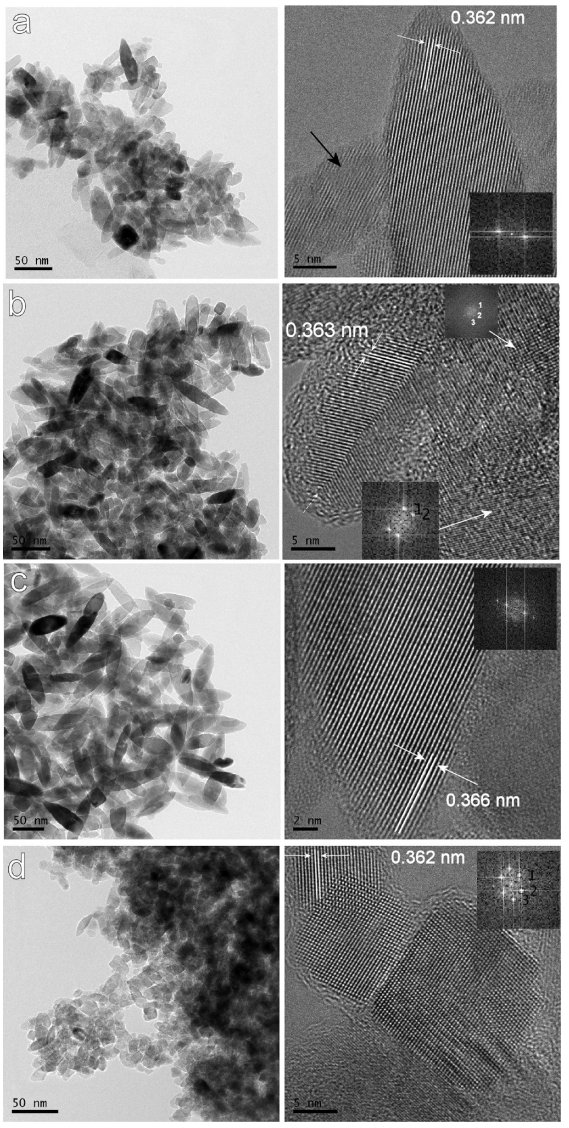

Figure 4. HRTEM photographs of W-doped titania: (a) TiW005; (b) TW010; (c) TiW015; (d) TiW025.

ratio of anatase particles decreased gradually with the addition of W and their morphology change from spindlelike to rectangular or squarelike shapes. The HRTEM image confirms that all particles possess an anatase structure with the *c* axis of the tetragonal symmetry collinear with the long axis of the spindle, as indicated by the crystal planes. The interlayer spacings *d* of the anatase crystal are in the range of 0.362−0.366 nm, which corresponds to the expanded lattice of anatase as calculated by Rietveld refinement from the XRD data.

The anatase nanocrystals (Figures 4a,c and 5a) show only a lattice spacing of ~0.36 nm, which can be assigned to plane (101) and corresponds to the basic shape of the anatase tetragonal {101} bipyramid (see Figure 6a).[39]

Twinning of the anatase crystals is a result of two subgrains sharing a common crystallographic plane; thus, the structure of one subgrain is the mirror reflection of the other by the twin plane. Figure 4b is a HRTEM image of a W-doped titania particle, which is composed of two such grains connected at a twin relation; the two inset fast Fourier transform (FFT) patterns

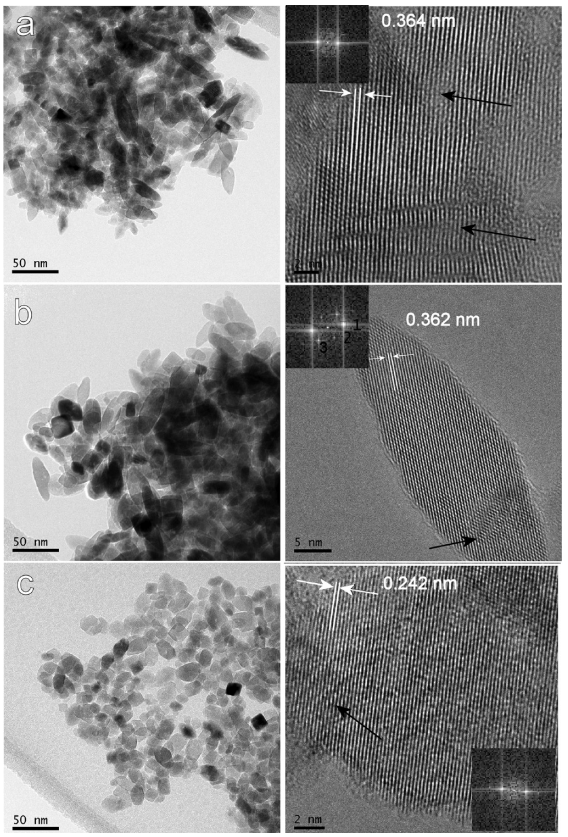

Figure 5. HRTEM photographs of W-doped titania: (a) TiW050; (b) TiW100; (c) TiW200.

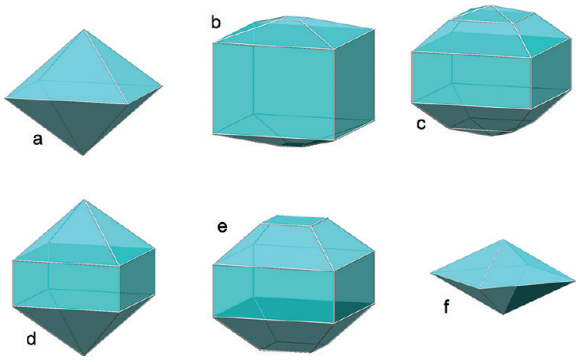

Figure 6. Morphology of possible anatase nanocrystals.

shows spots 1−3 with d spacings d_{100} = 0.371 nm, d_{004} = 0.237 nm, d_{103} = 0.243 nm, d_{100} = 0.382 nm, and d_{101} = 0.352 nm. These planes can be assigned to anatase crystal forms with facets {010} and {013}, as shown in Figure 6b,d. The twin planes are mirror symmetric with respect to the boundary indicated by a white dashed arrow.

The inset image of the FFT pattern was obtained from HRTEM (see Figure 4d), where spots 1−3 have d spacings of 0.381, 0.354, and 0.249 nm, respectively. These values demonstrate the lattice expansions of the W-doped titania specimens; spot 1 can be assigned to the (100) plane, and spot 2 corresponds to (101) and spot 3 to (103) atomic planes with lattice spacings of d_{100} = 0.378 nm, d_{101} = 0.352, and d_{103} = 0.243 nm in pure anatase (PDF 21-1272); the shape of the anatase crystal is given in Figure 6c.

The spindlelike anatase nanocrystals in Figure 5b show lattice spacings from FFT of d_{101} = 0.361 nm for the (101) plane, d_{100} = 0.382 nm for the (100) plane, and d_{002} = 0.491 nm for the (002) plane. This result indicates that the basal plane of the anatase nanocrystals corresponds to the (010) plane, which is perpendicular to the [010] direction. This result suggested that these anatase nanocrystals have a large aspect ratio of width to thickness.[40] The above results reveal that the anatase nanocrystals prepared in this study preferentially expose the (010) plane (see Figure 6e). Figure 5c depicts an interlayer spacing of d = 0.242 nm, which can be assigned to an expanded lattice of the (112) plane, and it corresponds to the basic shape of the anatase tetragonal {112} bipyramid (see Figure 6f).

The black arrows in Figures 4a,b and 5a,c indicate distortions[41] and dislocations[42] on the anatase [101] face. These distortions and dislocations were possibly attributed to electric stress, which may have originated from W ion doping.

Such doped anatase nanocrystals have a large aspect ratio of length to width and can be influenced by the amount of dopant. The growing amount of dopant leads to growth of the {010} planes (facets) at the expense of {101} and thus changes the morphology of the anatase crystal. The growth of {010} is ultimately reflected in the increase of the photocatalytic activity.[43,44]

3.3. Possible Forms of W in the Titania Structure. Considering the ionic size and oxidation state of the W^{6+} dopant, the following defect states can be proposed in accordance with the Kröger−Vink notation[45] similar to using Mo,[46] when (2) the incorporation of dopants creates conduction band electrons, (3) instead of creating conduction electrons, when charge compensation is also achieved by defects such as interstitial O atoms, or (4) when oxides are completely soluble and then the dopants occupy a substitution site, creating O vacancies.

$$WO_3 \leftrightarrow W_{Ti}^{\bullet\bullet} + 2Oo + 2e^- + \frac{1}{2}O_2 \quad (1)$$

$$W_2O_6 \leftrightarrow 2W_{Ti}^{\bullet\bullet} + 4Oo + 4e^- + O_2 \quad (2)$$

$$W_2O_6 \leftrightarrow 2W_{Ti}^{\bullet\bullet} + O^{\circ\circ} + 4Oo \quad (3)$$

$$W_2O_6 \leftrightarrow 2W_{Ti}^{\bullet\bullet} + 2Vo^{\circ\circ} + 4Oo \quad (4)$$

The imbalance in the charge created by doping can also be compensated for by Ti vacancies:

$$2W_2O_6 \leftrightarrow 4W_{Ti}^{\bullet\bullet} + 2V_{Ti}^{\circ\circ\circ\circ} + 12Oo \quad (5)$$

where WTi is a W ion at a Ti lattice site, Oo is O occupying an O lattice site, V_{Ti} is an Ti vacancy, Vo is an O vacancy, • represents the excess charge, and ° represents a deficiency in the charge.

3.4. Spectral Properties and Band Gap. Figure 7a depicts UV/vis absorption spectra of the as-prepared samples of W-doped titania. Anatase samples doped by W have new optical properties, which are different from both the titania and tungsten(VI) oxide. The anatase has a wide absorption band ranging from 200 to 385 nm, and WO_3 has a UV absorption band close to 400 nm.[47]

The reflectance data obtained are the percentage of reflected light compared with a nonabsorbing material ($BaSO_4$).

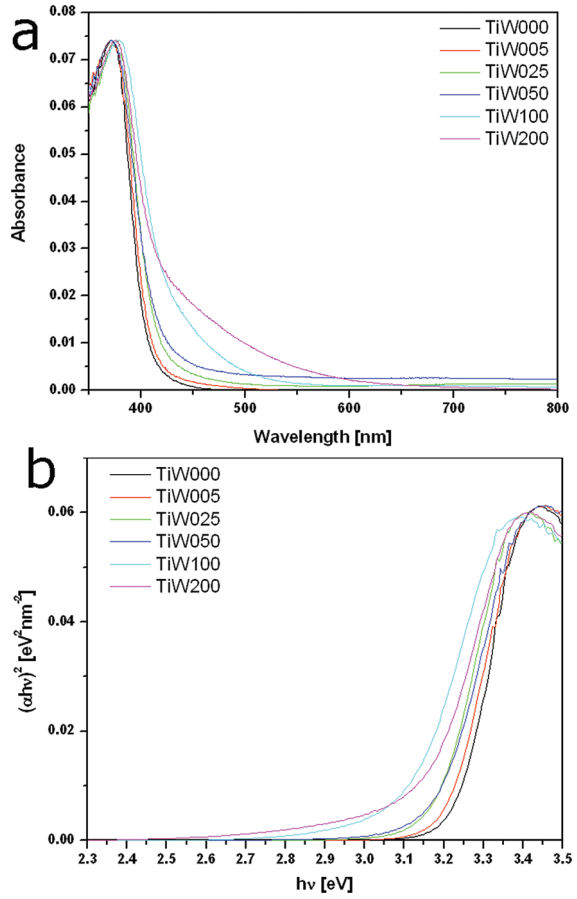

Figure 7. (a) UV/vis absorbance spectra of W-doped titania. (b) Band-gap energy of W-doped titania.

The Kubelka–Munk theory is generally used for recalculation of the diffuse reflectance of weakly absorbing samples to absorbance A:

$$A(R) = (1 - R)^2/2R \quad (6)$$

where R is the reflectance of the "infinitely thick" layer of the solid.[48]

Compared with pure titania, the absorption edge of the doped samples is red-shifted; the absorption tail extends to ~420 nm, as shown in Figure 7a. With an increase in the content of W, the prepared samples acquire a yellowish tinge, while the sample marked TiW200 is pale yellow.

The method of UV/vis diffuse-reflectance spectroscopy was employed to estimate band-gap energies of the doped titania samples. To establish a type of band-to-band transition in these synthesized particles, the absorption spectra were fitted to equations for direct band-gap transitions. The minimum wavelength required to promote an electron depends upon the band-gap energy E_{bg}, which is commonly estimated from UV/vis absorption spectra by the linear extrapolation of the absorption coefficient to zero using the following equation:

$$A(h\nu) = B(h\nu - E_{bg})^n \quad (7)$$

where A is the absorption according to eq 6, B is the absorption coefficient, and $h\nu$ is the photon energy in electronvolts calculated from the wavelength λ in nanometers[49,50]

$$h\nu = 1239/\lambda \quad (8)$$

If the fundamental absorption of the titania crystal possesses an indirect transition between bands, then $n = 2$ is for the direct transition between bands $n = {}^1/_2$.[51,52] The energy of the band gap is calculated by extrapolating a straight line to the abscissa axis, when α is zero, i.e., $E_{bg} = h\nu$.[53] Figure 7b shows $(Ah\nu)^2$ versus the photon energy for a direct band-gap transition and $(Ah\nu)^{1/2}$ versus E_{bg} for an indirect band-gap transition. The resulting extrapolated values of E_{bg} for indirect transitions are listed in Table 2. The value of 3.20 eV for the sample denoted as TiW000 is similar to that reported in the literature for pure anatase nanoparticles.[52,54] The value of the band-gap energy decreases with an increase in the content of the W dopant. The band gap of bulk WO_3 is 2.5 eV, which corresponds to absorption out to approximately 500 nm.

3.5. Photocatalytic Properties. The photocatalytic activity of the prepared samples was determined using degradation of 0.02 M Orange II dye aqueous solutions under UV radiation at 365 nm (UV-A, black lamp) and up 400 nm (warm white lamp). In regions where the Lambert–Beer law is valid, the concentration of the Orange II dye is proportional to absorbance:

$$A = \varepsilon cl \quad (9)$$

where A is the absorbance, c is the concentration of an absorbing component, l is the length of the absorbing layer, and ε is the molar absorption coefficient. Orange II dye does not undergo direct (noncatalyzed) photolysis, and any change in the Orange II dye concentration can only be attributed to heterogeneous photocatalysis. Figure S5 in the Supporting Information shows the typical time dependence of the visible-light absorbance due to Orange II dye degradation under $\lambda = 365$ nm irradiation. It should be noted that the intensity of the main absorption peak at $\lambda_{max} = 480$ nm decreases continuously with the time of increasing irradiation.

Photodegradation experiments of Orange II dye by the catalytic process exhibited first-order kinetics with respect to the concentration of the dye. The time dependence of Orange II dye decomposition can be described by using eq 10 for a reaction following first-order kinetics:

$$dc/dt = k(c_0 - c) \quad (10)$$

where C is the concentration of Orange II dye, C_0 is the initial concentration of Orange II dye, and k is the rate constant. The calculated degradation rate constants k (min^{-1}) are shown in Table 2, and the kinetics of degradation of Orange II dye at 365 nm (black light) and 400 nm (warm white) on samples TiW005–TiW200 are illustrated in Figure 8.

As can be seen in Table 2, doping of W increases the photocatalytic activity in both the UV and visible regions. The low activity of the nondoped sample is due to low crystallinity and the presence of amorphous domains.[55] The best photocatalytic activity in the UV region ($k = 0.06197$ min^{-1}) is achieved with the sample TiW030, which contains 3.37 wt % of W. The decrease in the photocatalytic activity of samples TiW010 and TiW015 compared to sample TiW005 is given by the content of the micropores in these samples. A further increase of the W content leads to a decline of the photocatalytic activity in the UV region.

As indicated in Table 2, the nondoped anatase (sample TiW000) exhibits very low visible-light photocatalytic activity for degradation of Orange II dye. The low photocatalytic activity of titania in the visible region is caused by an excessively high band-gap energy of pure anatase (3.2 eV, $\lambda_{bg} = 388$ nm) and rutile (3.0 eV, $\lambda_{bg} = 413$ nm).[52] All prepared W-doped samples

Table 2. Band-Gap Energy, Rate Constant k, and k/BET for UV and Visible Light

sample	band gap [eV]	k 365 nm [min^{-1}]	k 400 nm [min^{-1}]	k/BET 365 nm [$min^{-1}/m^2\ g^{-1}$]	k/BET 400 nm [$min^{-1}/m^2\ g^{-1}$]
TiW000	3.2	0.007 30	0.002 00	5.03×10^{-5}	1.37×10^{-5}
TiW005	3.1	0.032 79	0.003 21	1.80×10^{-4}	1.76×10^{-5}
TiW010	3.1	0.031 43	0.008 40	3.12×10^{-4}	8.35×10^{-5}
TiW015	3.0	0.025 55	0.004 68	2.15×10^{-4}	3.94×10^{-5}
TiW017	3.0	0.026 36	0.004 64	2.10×10^{-4}	3.70×10^{-5}
TiW020	3.0	0.041 26	0.005 91	4.42×10^{-4}	6.33×10^{-5}
TiW022	2.9	0.021 29	0.003 69	1.32×10^{-4}	2.29×10^{-5}
TiW025	2.9	0.029 17	0.006 14	2.28×10^{-4}	4.79×10^{-5}
TiW030	2.8	0.061 97	0.011 00	4.09×10^{-4}	7.25×10^{-5}
TiW050	2.8	0.035 90	0.005 07	3.01×10^{-4}	4.25×10^{-5}
TiW100	2.7	0.025 29	0.005 00	2.43×10^{-4}	4.80×10^{-5}
TiW125	2.7	0.047 54	0.007 08	2.24×10^{-4}	3.34×10^{-5}
TiW150	2.6	0.045 96	0.004 99	1.90×10^{-4}	2.07×10^{-5}
TiW175	2.6	0.044 18	0.005 44	2.29×10^{-4}	2.81×10^{-5}
TiW200	2.6	0.039 62	0.002 93	3.40×10^{-4}	2.51×10^{-5}

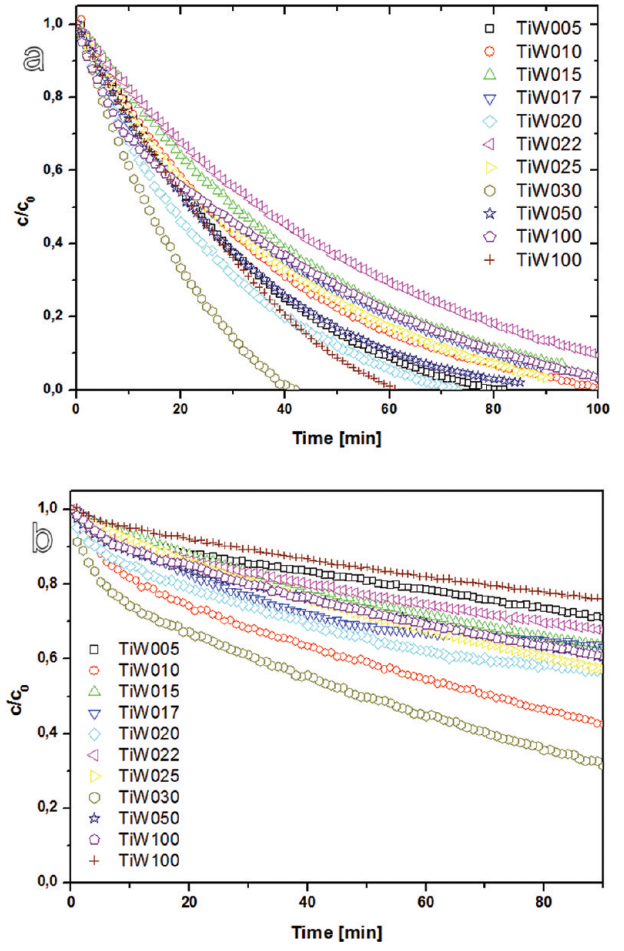

Figure 8. Orange II dye degradation on W-doped titania at wavelengths (a) 365 and (b) 400 nm.

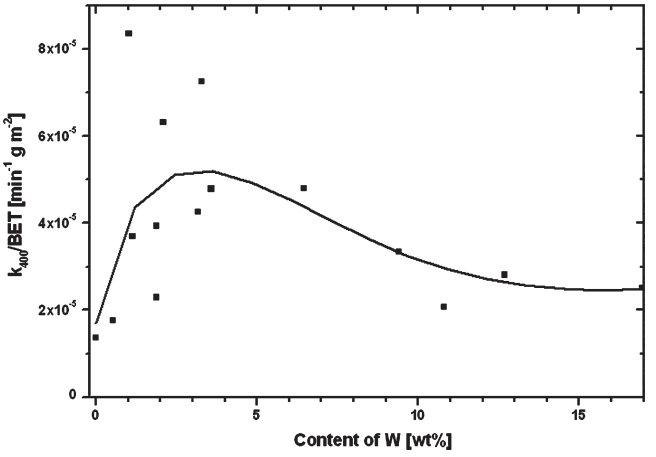

Figure 9. BET surface-area-normalized reaction rate constants plotted against the content of W. Line: Weibull function fit of experimental data smoothed by 2-point adjacent averaging.

have higher activity than the nondoped sample (TiW000) in irradiation by visible light (Figure 9), which can be partly attributed to the lower band-gap energy (see Table 2) but also to structural and crystal habit changes. The best photocatalytic activity at the visible-light region again has been achieved with the sample labeled TiW030 (k = 0.0110 min^{-1}).

The band-gap energy increase is not the only factor limiting the catalytic performance: the specimens with >3 wt % W have the lowest E_{bg} but are comparably active as W-free titania. The catalysts with the best performance have a medium W content (1.0−3.3 wt %), where the W-doped anatase had a local minimum of the a lattice cell and cell volume, all of which could point to the smallest concentration of structural departures from the pure anatase. The accompanying effect of the crystal-shape changes, inferred from more diffraction planes observed in SAED patterns in W-doped titanias, can also contribute to the fact that the specimens with the lowest E_{bg} are not actually the most active ones. W doping, hence, affects more relevant features of titania than only its electronic structure.

4. CONCLUSION

The W-doped titania samples were prepared by thermal hydrolysis of titanium and tungsten peroxo complexes in aqueous

solutions. The prepared monodisperse anatase particles have a mesoporous character with a pore-size distribution of 10−15 nm. W doping affects the anatase structure, which is demonstrated by changes in the unit cell, Raman spectra, and band-gap energy. The W addition causes a red shift of the optical absorption related to a decrease of the band-gap energy, which increases the photocatalytic activity of titania after UV radiation as well as in the visible-light region with respect to undoped titania. The best performance in Orange II dye photocatalytic decomposition was achieved at medium W doping, i.e., with samples that have the smallest anatase unit cell.

Thermal hydrolysis of the peroxo complex has one great advantage compared with other synthesis reactions, namely, that it is a "one-pot" reaction with easily accessible chemicals and the reaction residue is water, not organic wastes. This could be promising for possible future technological use.

■ ASSOCIATED CONTENT

Supporting Information. XRD diffractogram, results of Rietveld refinement, IR spectra, BJH pore size distribution plots, and typical UV/vis absorbance spectra. This material is available free of charge via the Internet at http://pubs.acs.org.

■ AUTHOR INFORMATION

Corresponding Author

*E-mail: stengl@iic.cas.cz. Tel.: 420 2 6617 2193. Fax: 420 2 2094 0157.

■ ACKNOWLEDGMENT

This work was supported by the Academy of Sciences of the Czech Republic (Project AV OZ 40320502) and the Czech Science Foundation (Project 203/08/0334). The authors gratefully acknowledge the assistance of Ing. N. Murafa for HRTEM measurements and Dr. P. Bezdička for XRD measurements.

■ REFERENCES

(1) Yang, H.; Zhang, D.; Wang, L. *Mater. Lett.* **2002**, *57*, 674–678.
(2) Lorret, O.; Francova, D.; Waldner, G.; Stelzer, N. *Appl. Catal., B* **2009**, *91*, 39–46.
(3) Couselo, N.; Einschlag, F. S. G.; Candal, R. J.; Jobbagy, M. *J. Phys. Chem. C* **2008**, *112*, 1094–1100.
(4) Hathway, T.; Rockafellow, E. M.; Oh, Y. C.; Jenks, W. S. *J. Photochem. Photobiol., A* **2009**, *207*, 197–203.
(5) Eibl, S.; Gates, B. C.; Knozinger, H. *Langmuir* **2001**, *17*, 107–115.
(6) Tryba, B.; Piszcz, M.; Morawski, A. W. *Int. J. Photoenergy* **2009**.
(7) Ortiz-Islas, E.; Lopez, T.; Gomez, R.; Picquart, M.; Aguilar, D. H.; Quintana, P. *Appl. Surf. Sci.* **2005**, *252*, 853–857.
(8) Lee, Y. C.; Hong, Y. P.; Lee, H. Y.; Kim, H.; Jung, Y. J.; Ko, K. H.; Jung, H. S.; Hong, K. S. *J. Colloid Interface Sci.* **2003**, *267*, 127–131.
(9) Tsai, H. L.; Leung, L. K. H.; Li, G. S.; Leung, D. C. Y. *MRS Proc.* **2010**, *1258* (1258), Q05–06.
(10) Rampaul, A.; Parkin, I. P.; O'Neill, S. A.; DeSouza, J.; Mills, A.; Elliott, N. *Polyhedron* **2003**, *22*, 35–44.
(11) Yang, Y.; Wang, H.; Li, X.; Wang, C. *Mater. Lett.* **2009**, *63*, 331–333.
(12) Song, K. Y.; Park, M. K.; Kwon, Y. T.; Lee, H. W.; Chung, W. J.; Lee, W. I. *Chem. Mater.* **2001**, *13*, 2349–2355.
(13) Cerny, Z.; Stengl, V. CZ200800139-A3 and CZ301006-B6, 2008.
(14) Zhao, W. R.; Shi, H. X.; Wang, D. H. *Chemosphere* **2004**, *57*, 1189–1199.
(15) Demirev, A.; Nenov, V. *Ozone: Sci. Eng.* **2005**, *27*, 475–485.
(16) Stylidi, M.; Kondarides, D. I.; Verykios, X. E. *Appl. Catal., B* **2004**, *47*, 189–201.
(17) JCPDS PDF 2 Database, Release 50, International Centre for Diffraction Data, Newtown Square, PA, 2000.
(18) ICSD Database FIZ, Karlsruhe, Germany, 2008.
(19) Brunauer, S.; Emmett, P. H.; Teller, E. *J. Am. Chem. Soc.* **1938**, *60*, 309–319.
(20) Barrett, E. P.; Joyner, L. G.; Halenda, P. P. *J. Am. Chem. Soc.* **1951**, *73*, 373–380.
(21) Orel, Z. C.; Gunde, M. K.; Orel, B. *Prog. Org. Coat.* **1997**, *30*, 59–66.
(22) Lachheb, H.; Puzenat, E.; Houas, A.; Ksibi, M.; Elaloui, E.; Guillard, C.; Herrmann, J. M. *Appl. Catal., B* **2002**, *39*, 75–90.
(23) Monteagudo, J. M.; Duran, A. *Chemosphere* **2006**, *65*, 1242–1248.
(24) Stengl, V.; Houskova, V.; Bakardjieva, S.; Murafa, N.; Havlin, V. *J. Phys. Chem. C* **2008**, *112*, 19979–19985.
(25) Aryanpour, M.; Hoffmann, R.; DiSalvo, F. J. *Chem. Mater.* **2009**, *21*, 1627–1635.
(26) Bakardjieva, S.; Subrt, J.; Stengl, V.; Dianez, M. J.; Sayagues, M. J. *Appl. Catal., B* **2005**, *58*, 193–202.
(27) Stengl, V.; Bakardjieva, S. *J. Phys. Chem. C* **2010**, *114*, 19308–19317.
(28) Zhang, H. Z.; Banfield, J. F. *J. Phys. Chem. B* **2000**, *104*, 3481–3487.
(29) Devi, S.; Jha, A. K. *Phys. B (Amsterdam, The Neth.)* **2009**, *404*, 4290–4294.
(30) Pullar, R. C.; Penn, S. J.; Wang, X.; Reaney, I. M.; Alford, N. M. *J. Eur. Ceram. Soc.* **2009**, *29*, 419–424.
(31) Kamisaka, H.; Suenaga, T.; Nakamura, H.; Yamashita, K. *J. Phys. Chem. C* **2010**, *114*, 12777–12783.
(32) Shao, G. S.; Zhang, X. J.; Yuan, Z. Y. *Appl. Catal., B* **2008**, *82*, 208–218.
(33) Ding, Z.; Lu, G. Q.; Greenfield, P. F. *J. Phys. Chem. B* **2000**, *104*, 4815–4820.
(34) Connor, P. A.; Dobson, K. D.; McQuillan, A. J. *Langmuir* **1999**, *15*, 2402–2408.
(35) Soler-Illia, G.; Louis, A.; Sanchez, C. *Chem. Mater.* **2002**, *14*, 750–759.
(36) Jere, G. V.; Patel, C. C. *Can. J. Chem.* **1962**, *40*, 1576–1582.
(37) Lowell, S.; Shields, J. E. *Powder Surface Area and Porosity*; Delft University of Technology: Delft, The Netherlands, 1998.
(38) de Boer, J. A.; *Structure & Properties of Porous Materials*; Butterworths: London, 1958.
(39) Barnard, A. S.; Zapol, P. *J. Phys. Chem. B* **2004**, *108*, 18435–18440.
(40) Wen, P. H.; Itoh, H.; Tang, W. P.; Feng, Q. *Langmuir* **2007**, *23*, 11782–11790.
(41) Liu, F. M.; Ding, P.; Yang, X. A.; Li, J. Q. *Nucl. Instrum. Methods Phys. Res., Sect. B* **2009**, *267*, 3104–3108.
(42) Liu, Z. L.; Cui, Z. L.; Zhang, Z. K. *Mater. Charact.* **2005**, *54*, 123–129.
(43) Pan, J.; Liu, G.; Lu, G. Q.; Cheng, H.-M. *Angew. Chem., Int. Ed.* **2011**, *50*, 2133–2137.
(44) Pan, J.; Wu, X.; Wang, L.; Liu, G.; Lu, G. Q.; Cheng, H.-M. *Chem. Commun.* **2011**, *47*, 8361–8363.
(45) Kroger, F. A.; Vink, H. J. *Solid State Physics*; Academic Press: New York,1956; Vol. 3.
(46) Gomathi Devi, L.; Narasimha Murhty, B.; Girish Kumar, S. *Catal. Lett.* **2009**, *130*, 496–503.
(47) Asim, N.; Radiman, S.; Yarmo, M. A. B. *Am. J. Appl. Sci.* **2009**, *6*, 1424–1428.
(48) Christy, A. A.; Kvalheim, O. M.; Velapoldi, R. A. *Vib. Spectrosc.* **1995**, *9*, 19–27.
(49) Reddy, K. M.; Manorama, S. V.; Reddy, A. R. *Mater. Chem. Phys.* **2003**, *78*, 239–245.
(50) Tauc, J.; Grigorov, R.; Vancu, A. *Phys. Status Solidi B* **1966**, *15*, 627–637.

(51) Reyes-Coronado, D.; Rodriguez-Gattorno, G.; Espinosa-Pesqueira, M. E.; Cab, C.; de Coss, R.; Oskam, G. *Nanotechnology* **2008**, 19.
(52) Serpone, N.; Lawless, D.; Khairutdinov, R. *J. Phys. Chem.* **1995**, *99*, 16646–16654.
(53) Sanchez, E.; Lopez, T. *Mater. Lett.* **1995**, *25*, 271–275.
(54) Bhatkhande, D. S.; Pangarkar, V. G.; Beenackers, A. *J. Chem. Technol. Biotechnol.* **2002**, *77*, 102–116.
(55) Murafa, N.; Stengl, V.; Houskova, V. *Microsc. Microanal.* **2009**, *15*, 1036–1037.